Computers and Geotechnics 173 (2024) 106563

Contents lists available at ScienceDirect

Computers and Geotechnics

journal homepage: www.elsevier.com/locate/compgeo

Research Paper

Large deformation numerical assessment of rock anchor response under axial loading for offshore renewable energy applications

Alessio Genco [a], Matteo Oryem Ciantia [a,d,*], Marco Previtali [a], Michael Brown [a], Ana Ivanovic [b], Nick Cresswell [c], Vincent Twomey [c]

[a] School of Science and Engineering, University of Dundee, Dundee, UK
[b] School of Engineering, University of Aberdeen, Aberdeen, UK
[c] SCHOTTEL Marine Technologies, Edinburgh, UK
[d] Department of Earth and Environmental Sciences, University of Milano-Bicocca, Italy

ARTICLE INFO

Keywords:
Rock anchor
Geotechnical-particle-finite-element modelling
Offshore geotechnical engineering
Rate effects
Hydro-mechanical coupling

ABSTRACT

The study presented in this paper aims to advance the current understanding of Rock Anchor (RA) performance under axial loading through large deformation numerical analyses. Simulations are conducted using the Geotechnical Particle Finite Element Method within a coupled hydro-mechanical framework. Experimental data from the literature is used to calibrate a strain hardening plasticity constitutive model for rocks. The calibrated model is then used to investigate rate effects on the axial response of a novel rock anchor design. The axial pullout induces rock dilatation at the bottom edge of the anchor with the consequent formation of a zone of negative water pressure change and a bulb of positive pore water pressure change above it. Depending on the pullout rate, distinct drained, partially drained, and undrained hydraulic regimes are identified. These, along with the variable damage distributions, are shown to influence the rock anchor axial capacity considerably. The geometrical and elastic properties of the rock anchor modelled as a deformable body, along with the interface friction angle between the anchor and the rock are also explored. Results such as load capacity curves, stress path evolutions, and stress distributions on the rock-rock anchor interface are analysed emphasizing their impact on rock anchor design.

1. Introduction

The expansion of Offshore Renewable Energy (ORE) necessitates the development of anchoring solutions that are both cost-effective and reliable, requiring a robust design approach that transcends the limitations of traditional methods. The offshore environment is characterized by the challenging dynamics of tidal and wind forces, where floating devices anchored to the seabed face complex loading conditions. Rock Anchors (RAs) are specifically designed to account rocky seabeds characterized by various types and conditions.

Traditionally, the design procedure of rock anchors is based upon analytical and empirical methods assuming the cone pull-out mechanism, where the load capacity is normally equivalent to the weight of the failing rock wedge formed and the tensile strength acting normally to the failure surface (Weerasinghe and Littlejohn, 1997). This approach, which is widely used to date and revealed conservative because of the assumptions involved, was expanded by integrating Limit Analysis (LA) methods enhancing RA design under axial loading (Brown, 2015; Kim and Cho, 2012; Serrano and Olalla, 1999; Yap and Rodger, 1984). Consequently, the numerical approach has become a widely adopted tool for evaluating rock anchor interaction problems easily by means of parametric analysis. Cerfontaine et al. (2021) performed parametric LA simulations to assess the influence of rock properties and anchor geometry on the anchor capacity, confirming the conservatism of the analytical approach suggested by existing design procedures (Yap and Rodger, 1984). Finite Element Methods (FEMs) which do not rely on a-priori assumptions on the failure geometry (Griffiths and Lane, 1999) were adopted to advance the understanding of the rock anchor failure mechanism enabling the localisation of plastic shear strains and consequent propagation of the failure. Yap and Rodger (1984) used a FEM model to investigate the axial response of grouted rock anchors revealing the formation of different failure mode based on the anchor embedment depth (H/D). Discontinuum approaches have also been widely adopted for the simulation of the crack fracture propagation in rock accounting for the anisotropic nature of this material. Panton et al.,

* Corresponding author at: Geotechnical Division, School of Science and Engineering, University of Dundee, DD1 4HN, Nethergate, Dundee, United Kingdom.
E-mail addresses: m.o.ciantia@dundee.ac.uk, matteo.ciantia@unimib.it (M.O. Ciantia).

https://doi.org/10.1016/j.compgeo.2024.106563

Available online 4 July 2024

Nomenclature

$\boldsymbol{b}$	external body force tensor
c	linear proportional factor between P_t and P_m
c_h	horizontal coefficient of consolidation
d	dilatancy
D	anchor shaft diameter
e_0	initial void ratio
E	Young's modulus
f	yield surface function
$f(x)$	local field
$\boldsymbol{F}$	deformation gradient
$\overline{F}_y$	normalized pull-out capacity
g	plastic potential function
h	height of the anchor fingers
H	total height of the anchor
H/D	embedment depth
J	Jacobian of the deformation gradient
J_2	deviatoric stress invariant
k	permeability
k_w	hydraulic conductivity
$\boldsymbol{l^p}$	spatial plastic velocity
l_s	length scale parameter
M_f and M_g	controls the slope of the critical line for the yield envelope and plastic potential
$\mathrm{M_n}$	mesh at a specific calculation step
$\boldsymbol{p_w}$	Cauchy water tensor
P_t, $P_s$andP_m	internal hardening variables
P_{t0}	initial tensile strength
P' and Q	geotechnical stress invariants
t_n	time at a specific calculation step
$w(x,\xi)$	weighting function
v	pullout velocity
V_C	normalised velocity
v and v^d	solid skeleton and Darcy' velocity
$\mathrm{V_n}$	volume at a specific calculation step
α	inclination of the anchor fingers
γ_w	bulk water density
Δu	excess of pore water pressure
δ	interface friction angle
ε_{vol} and ε_a	volumetric and axial strains
η^*	stress ratio
θ	scalar volumetric deformation
λ	compressibility index
ν	Poisson's ratio
ρ_s, ρ_t, χ_s and χ_t	constitutive hardening parameters
$\boldsymbol{\sigma}$	Cauchy stress tensor
σ'_{v0}	effective vertical stress
σ'_n	effective normal stress
τ	tangential stress

(2015) performed Distinct Element (DE) simulations underscoring the impact of the spatial distribution of joints in rock masses on the fracture propagation and the load capacity of grouted RAs. These findings confirm that the anchor geometric properties and relative stiffness between rock-anchor crucially affect the failure mode.

According to Brown (2015) failure mechanisms of the RA under axial loading can be synthesized into three categories: (a) Deep failure mechanism, (b) interface failure mechanism, and (c) cone failure mechanism. *Deep failure mechanisms* occur at greater embedment depths (Littlejohn et al., 1978) where localised damage around the anchor tip is sufficient to fail the anchor. The *interface failure mechanism* results from the frictional slip at the rock-anchor interface. Such a failure mode happens if the anchor head is not sufficiently fixed to the rock or if local damage causes the anchor head to slip vertically. Critical factors influencing this process include interface friction, relative stiffness, and surface roughness, as well as confining pressure and dilatancy (Littlejohn et al., 1978; Brown, 2015; Ziogos et al., 2021; Frost et al., 2002). Ziogos et al. (2015) conducted extensive laboratory tests to evaluate the frictional behaviour of the steel-rock interaction and determine the interface friction angle (δ) across various rock types listed in Table 1, showing that stress state significantly affects the resulting friction angle (Ziogos et al., 2021). *Cone failure mechanisms* predominantly occur at low embedment ratios, where conical failure surfaces develop from the anchor tip towards the rock surface (Brown, 2015). Cerfontaine et al. (2021) highlighted that the bearing capacity of a deep mechanisms is independent of depth and that beyond a critical embedment depth, the failure transitions from deep to cone failure mechanism type. Nonetheless, to date the failure mechanism and shape of the cone is still not clear. Coates and Yu (1971) and Kim and Cho (2012) consider a conical failure mechanism (90° cone angle) while, Littlejohn et al. (1978) report that, depending on rock quality, the cone angle may be 60° for weathered and soft rocks or 90° for intact strong rocks. On the other hand Wyllie (1999) shows that this angle may reach up to 120° for strong rocks. These failure surface geometries were derived from field tests data although the rock structure assumes a relevant role on the rock fracture distribution. Limit Analysis methods assume curved failure surfaces limited at the top part of the anchor whereas the failure at the bottom is characterized by the interface mode (Serrano and Olalla, 1999; Zhao et al., 2018; Zhang et al., 2019).

Table 1
List of the basic interface friction angle δ for different rock types derived from Ziogos et al. (2021) extended following further tilt table testing.

	Interface steel-rock friction angle, δ: degrees
Calcarenite	25.0
Limestone	25.2
Chalk	30.0
Granite	30.0
Sandstone	30.5
Andesite	33.2
Flagstone	34.3

It is important to consider that most analytical and numerical models developed to date, are for onshore applications and based on experimental campaigns performed on dry rock or concrete. In the offshore environment the presence of water and the environmental actions introduce a new aspect that has not been investigated. Depending on rock porosity and the presence of fractures/fissures, the permeability of rock can typically vary from 1×10^{-18} to 1×10^{-10} m^2 (Bagdassarov, 2021). RAs will hence experience environmental loads causing the rock to sometimes respond in a drained, undrained, and partially drained manner. Wind and wave action can impose rapid loading rates on the anchors, which may result in an undrained or partially drained response of the rock (Chow et al., 2020). Partial drainage occurs when the water pressure distribution and its temporal evolution controls the effective stress distribution, Hydro-Mechanical (HM) coupled phenomena may ultimately determine the failure mechanism. Experimental results indicate that drainage conditions can play a governing role in deformation and fracture (Lei et al., 2011; Stanchits et al., 2009). As already observed for plate anchors in sand and clay, drainage may have a significant effect on RA capacity and failure modes. Nonetheless, these HM coupled processes may create challenges for offshore geotechnical engineering as they are difficult to analyse through field or experimental

physical modelling (Brown and Hyde, 2008).

Advanced numerical methods are therefore becoming an attractive solution to support field and laboratory testing for the improvement of RA design. In particular, the goal of this paper is to advance our understanding on the axial performance of RAs in the offshore environment through a numerical investigation. In particular the Geotechnical Particle Finite Element Method (G-PFEM) (Carbonell et al., 2022; Monforte et al., 2018) with a coupled hydro-mechanical formulation (Monforte et al., 2018), is used to investigates pullout rate effects or RA axial response. The soil structure interaction is modelled using the contact mechanics capabilities of the GPFEM. The rock is modelled using a Structured-Modified Cam Clay model (S-MCC) (Monforte et al., 2019). After calibrating the model against Berea sandstone data from the literature large deformation analyses of the tensile capacity of a RA under different hydraulic regimes, namely drained, partially drained, and undrained, are performed. To overcome a mesh dependent response, a non-local finite strain formulation was used (Oliynyk et al., 2021). The significance role of the interface friction angle and RA geometry on the axial capacity was investigated. It is shown that failure mechanisms inducing rock dilatation, lead to the formation of large negative pore water pressure (*pwp*) at the bottom edge of the anchor. The results underscore the imperative of accounting for hydro-mechanical coupled behaviour, a feature that is normally discounted and that cannot be incorporated in LA. It is also shown that geometrical properties and RA deformability can critically influence failure propagation and the capacity of rock anchors.

2. Methodology

2.1. The GPFEM

The G-PFEM (Oñate et al., 2004) employs a continuum-based approach for simulating large strain interaction problems (Monforte et al., 2017). Integrated into the Kratos Multiphysics platform (Dadvand et al., 2010), the Update Lagrangian formulation is implemented for the discretization of the domain, where static and kinematic variables referred to the last configuration performed, are computed by means of the finite strain theory. In G-PFEM the domain is discretized to solve the classic differential equations of the continuum mechanics, where mesh nodes are considered as particles free to move during the calculation (Fig. 1). A key feature of G-PFEM is the adoption of the Delaunay tessellation for reconnecting particles at each calculation step, providing an update boundary and mesh configuration. The alpha-shape method is adopted for recovering and update the previous boundary for a current configuration of the domain. Furthermore, the mesh adaptivity included in G-PFEM provides the addition of particles in regions where the threshold of a defined plastic state variable is overcome. In other words, as displayed in Fig. 1, cloud points at a specific time step (t_n) are defined, representing subsequent volume (V_n), and mesh discretization (M_n). As the simulation progresses to the next time step (t_{n+1}), the cloud point configuration is updated to reflect new boundaries, with additional particles introduced as needed, updating the mesh definition (Monforte et al., 2017). The remeshing technique described, effectively prevents the mesh tangling and distorting which negatively affect classic Lagrangian FEMs leading to convergence issues (Drescher and Detournay, 1993; De Borst and Vermeer, 1985). Recent applications of G-PFEM include various Boundary Value Problems (BVPs) that replicate experimental tests such as drained triaxial, oedometer, and biaxial tests, in addition to modelling shallow footings under vertical pressure, Cone Penetration Tests (CPTs), and the installation of open-ended piles in soft rocks (Monforte et al., 2019; Oliynyk et al., 2021; Ciantia, 2018; Previtali et al., 2023).

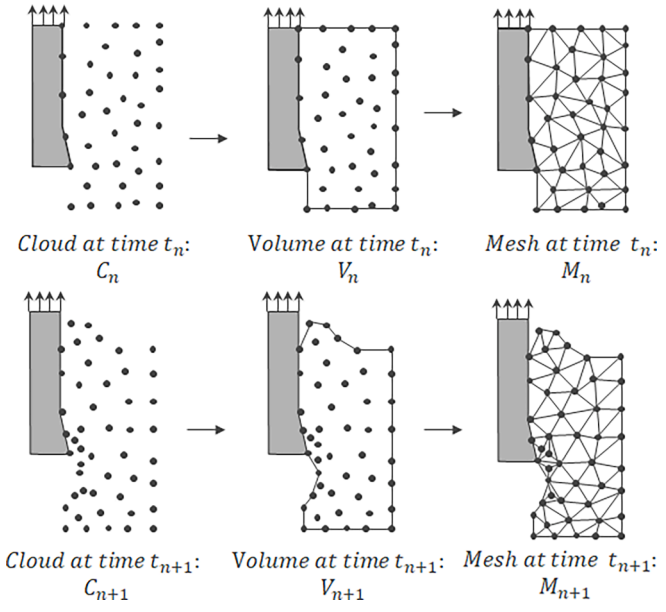

Fig. 1. Sequence of cloud, volume, and mesh configurations at time t_n and t_{n+1} representing the rock anchor pull-out under axial displacement.

2.2. Modelling the rock anchor – rock interaction

To model the rock-rock anchor interaction, two contact strategies are adopted. Expandable fingers (a key component of the rock anchor shown in Fig. 3) with inclination angle lower than 3°, are treated as a non-deformable boundary, employing the penalty approach for calculating the contact forces on the deformable rock (Huněk, 1993). Alternatively, the Contact Domain (CD) method is used, detecting contact during the remeshing/alpha shape step, and deploying ancillary elements to ensure consistent repulsion between materials with different stiffnesses via the Lagrangian multiplier approach. Tangential forces are then determined using Coulomb's law of friction. In both cases, contact stiffness is determined by multiplying the rock stiffness by a multiplying factor. This factor is chosen depending on the mesh size and displacement rate to minimise computational burden while avoiding geometry overlaps (Genco et al., 2022). In presence of water the coupled HM $\boldsymbol{u}-w-p_w$ (displacement – Darcy's water velocity or displacement – water pressure) framework was adopted, the model implements partially drained conditions by adding a water pressure degree of freedom to the mesh elements and including a term for water compressibility and pressure to the balance equations (Monforte et al., 2018).

In order to consider Terzaghi's effective stress principle to be applicable, in this work the porous sandstone rock was assumed fully saturated and Biot's coefficient $\alpha = 1$.

Pore pressure is redistributed using Darcy's law for fully saturated media. Therefore, unless a hydraulic boundary condition is applied (e.g. prescribed water pressure at the top of the rock domain), null Neumann conditions are imposed; that is: zero water flow at the interface (Monforte et al., 2018).

2.3. The non-local structured Modified Cam Clay model

To address the behaviour of structured materials and mitigate mesh-dependent responses, this study uses the large strain non-local Structured Modified Cam Clay (S-MCC) model, presented by Monforte et al. (2019). As the constitutive model itself is rate-independent, rate effects will purely emerge from the coupled hydromechanical response.

Following the original MCC formulation, the yield locus is elliptically shaped, incorporating a bonding-related internal variable (Fig. 2). The model adopts a non-associated flow rule, utilizing distinct parameter sets for the yield surface and the plastic potential, enhancing its ability to simulate the brittle and dilatant response of soft rocks (Ciantia, 2018).

The yield surface f and plastic potential g read:

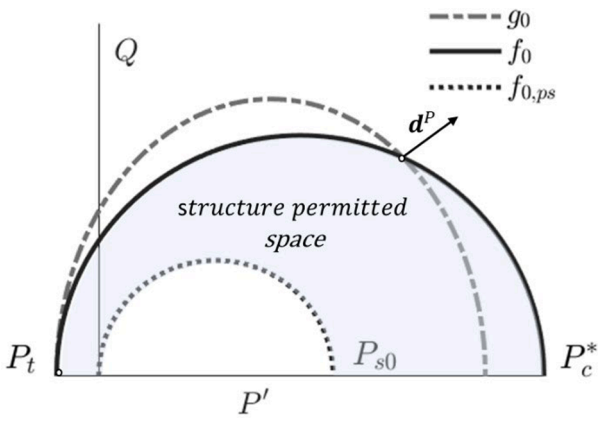

Fig. 2. The yield locus and the plastic potential function for the S-MCC model.

$$\begin{cases} f(\boldsymbol{\tau}', P_s, P_t, P_m) = \left(Q/M(\theta)_f\right)^2 + P^*\left(P^* - P_c^*\right) \\ g(\boldsymbol{\tau}', p_s, p_t, p_m) = \left(Q/M(\theta)_g\right)^2 + P^*\left(P^* - P_{c,g}^*\right) \end{cases} \tag{1}$$

where $P' = tr(\boldsymbol{\tau}')/3$, $Q = \sqrt{3J_2}$ and θ are the stress invariants. M_f controls the vertical extent of the yield function in the $Q : P'$ Kirchhoff stress invariant space while M_g the slope of the critical state line of the plastic potential function in the same $Q : P'$ space. P_t, P_s and P_m are internal hardening variables such that:

$$P_c^* = P_t + P_s + P_m = P_s + (1 + c)P_t \tag{2}$$

$$P^* = P' + P_t \tag{3}$$

where P_s acts as preconsolidation pressure of the reference unbonded material, whilst P_t and P_m (linear proportional through parameter c) indicate the tensile strength and the increase in the surface size due to tensile bonds, respectively. These two hardening parameters, which control the size of the yield surface, may tend to zero because of the destructuration effect driving to the formation of unstructured materials (Monforte et al., 2019). The hardening laws are defined as:

$$\dot{P}_s = \rho_s P_s \left((tr(\boldsymbol{l}^p) + \chi_s \sqrt{2/3}\, \|dev(\boldsymbol{l}^p)\| \right) \tag{4}$$

$$\dot{P}_t = -\rho_t P_t \left(|tr(\boldsymbol{l}^p)| + \chi_t \sqrt{2/3}\, \|dev(\boldsymbol{l}^p)\| \right) \tag{5}$$

where ρ_s, ρ_t, χ_s and χ_t are constitutive parameters and $\boldsymbol{l}^p = \partial g/\partial \boldsymbol{\tau}$ the spatial plastic velocity gradient which depends on $\boldsymbol{\tau}$ the Kirchoff stress tensor. It should be noted that the plastic volumetric compaction enables the increase of P_s whereas plastic dilatation produces a reduction of P_s (Genco et al., 2022). χ_s will hence control dilatancy at the limit state. As indicated by Lagioia and Nova (1995), $\chi_s \neq 0$ can be used in a phenomenological way to capture experimental trends induced by features such as grain crushing which may prevent for reaching the Critical State (CS) condition also for large shearing levels. In this work χ_s is set to 0, and therefore the plastic deformations in terms of dilatancy will vary with the stress ratio $\eta^* = Q/P'$ following the expression:

$$d = M_g\left(M_g/\eta^* - 1\right) \tag{6}$$

This expression implies:

$$\begin{cases} \eta^* = M_g \Rightarrow d = 0 \\ \eta^* \to 0 \Rightarrow d \to \infty \end{cases} \tag{7}$$

where $d = 0$ represents the critical state condition, whilst $d \to \infty$ indicates the purely isotropic stress state.

Strain localisation in brittle rock materials poses significant challenges for continuum-based approaches, leading to mesh dependency (Galavi and Schweiger, 2010; Hill, 1962). The G-PFEM addresses this issue through a non-local regularization technique, wherein the material behaviour at a point is influenced not only by its own state but also by neighbouring points (Mánica et al., 2018). This approach adopts an

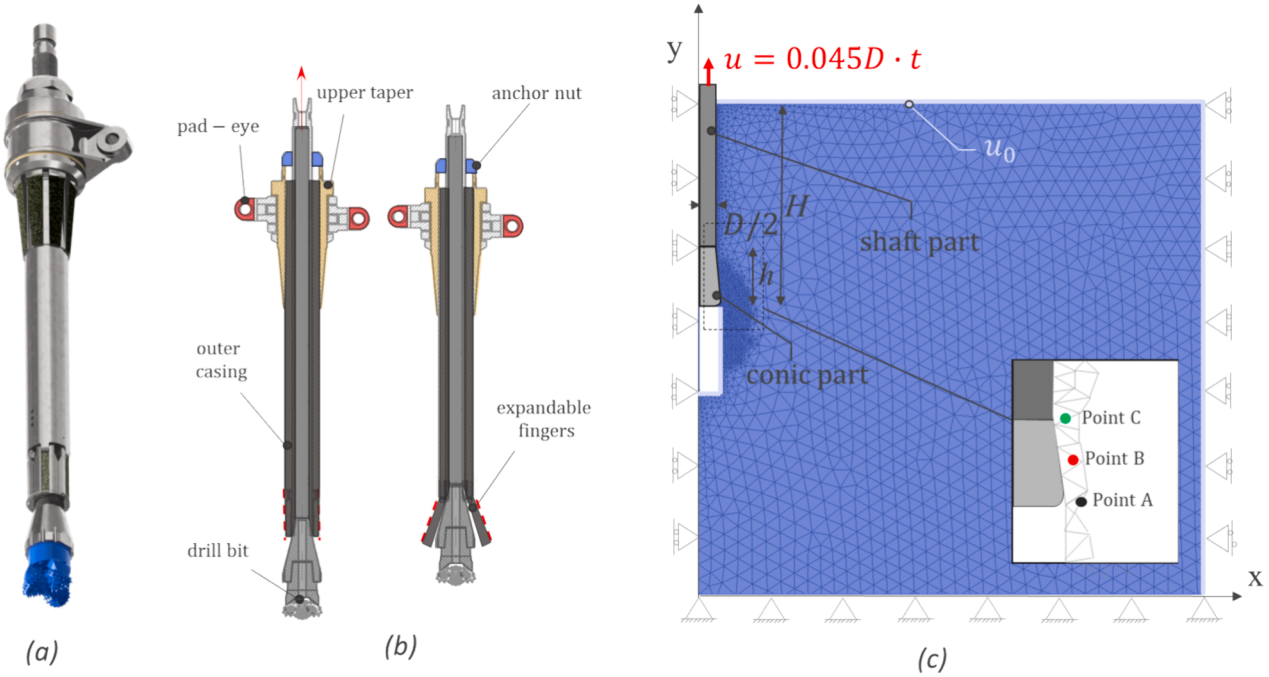

Fig. 3. a) 3d visualisation of the groutless anchor designed by SCHOTTEL Marine Technologies; b) schematic representing two subsequent phases of the installation procedure with main anchor components, and c) geometry of the rock anchor numerical model which shows the anchor geometry, the rock domain, the boundary constraints applied, and the refined mesh.

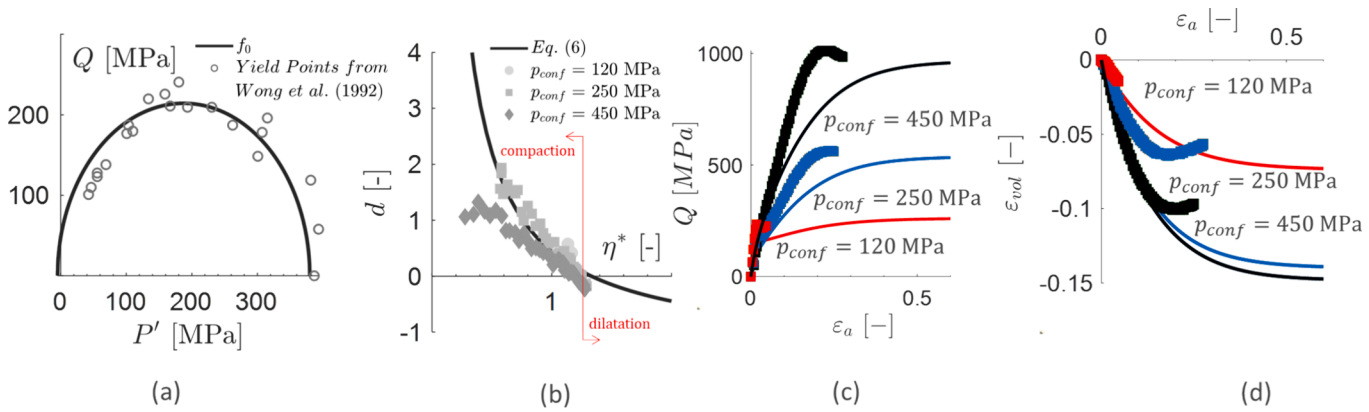

Fig. 4. a) calibration of the initial yield locus for the S-MCC model, b) variation of dilatancy with the stress ratio for the calibration of plastic potential parameters, and c) triaxial experimental data from Wong et al. (1992) represented by the markers while continuous lines the numerical model at three confinement pressure 450 MPa (black lines), 250 MPa (blue lines), and 120 MPa (red lines) in the $Q-\varepsilon_a$ plot, and d) $\varepsilon_{vol}-\varepsilon_a$ plot.

Table 2
Calibrated constitutive parameters for the S-MCC model.

E (MPa)	ν (−)	M_f(−)	M_g(−)	P_{s0}(MPa)	P_{t0}(MPa)	P_m(MPa)	ρ_s(−)	ρ_t(−)	χ_s(−)	χ_t(−)	l_s(cm)
16,800	0.20	1.00	1.25	200.00	5.00	180.00	14.00	14.00	0.00	0.01	1

Table 3
List of the simulation programme along with main test details.

TEST ID	k (m/s)	V_c (−)	δ (°)	α (°)	H/D (−)	E (kPa)
Reference	1×10^{-8} *1×10^{-3}	5.94×10^{5} 5.94×10^{0}	30	3	6	2.1×10^{8}
T_k	1×10^{-5} 1×10^{-6} 1×10^{-7} 1×10^{-8} 1×10^{-9} 1×10^{-10} 1×10^{-11} 1×10^{-12} 1×10^{-15} *1×10^{-18}	5.94×10^{2} 5.94×10^{3} 5.94×10^{4} 5.94×10^{5} 5.94×10^{6} 5.94×10^{7} 5.94×10^{8} 5.94×10^{9} 5.94×10^{12} 5.94×10^{15}	10 20 30	3	6	2.1×10^{8}
T_α	1×10^{-12}	5.94×10^{9}	30	3 6 10 15	6	2.1×10^{8}
$T_{H/D}$	1×10^{-12}	5.94×10^{9}	30	3	2 4 6 8 10	2.1×10^{8}
T_E	1×10^{-12}	5.94×10^{9}	30	3 6 10 15	6	2.1×10^{7} 11.5×10^{7} 2.1×10^{8}

*permeability values of used to achieve perfectly drained and fully undrained responses.

internal length scale parameter (l_s) which controls the size of the localised region. The parameter l_s can be experimentally calibrated, reflecting the observed shear band thickness and softening level (Mánica et al., 2020; Oliynyk et al., 2021; 2024). Beyond the interaction radius ($2l_s$) the interaction between Gauss points is assumed negligible, thus necessitating sufficient Gauss points within this radius to accurately compute non-local variables (Galavi and Schweiger, 2010). In this work the deviatoric and volumetric plastic strains are treated as non-local variables.

3. The rock anchor model and simulation programme

The anchor technology investigated here, provided by SCHOTTEL Marine Technologies (SMT), aims to reduce overall costs by means of a groutless solution, and self-drilling installation (Genco et al., 2022). Connected to a floating ORE platform via a pad-eye, this technology is proposed to provide cost reductions over traditional anchoring methods primarily due to the lower installation and operational cost (Cresswell et al., 2016). The anchor is made from steel, featuring a sacrificial self-drilling bit for the installation process, designed to minimize seabed disturbance and operational risks associated with offshore installations (Fig. 3a). It is composed of an outer casing with expandable fingers at the bottom, a taper at the top end and an inner stem with the lower drill bit (Fig. 3b). The drill bit allows for effective embedment into hard rocky seabeds, a process supported by an Anchoring Remotely Operated Vehicle. Upon reaching the design depth, the inner stem is retracted expanding the fingers which are in contact with the surrounding rock mass (Fig. 3b). To secure the anchor in place, a pre-tensioning is applied by tightening a nut on top ensuring the anchor stability (Cresswell et al., 2016).

Fig. 3c illustrates the geometry of the RA model which is idealized in axisymmetric conditions because of the symmetry of the numerical problem, thus representing only a slice of the entire domain. The anchor geometry, simplified as shaft and bottom part, was wished in place, as the present study does not address installation effects. The real size of the anchor has not been shown for commercial reasons. The domain size was chosen to minimize potential boundary effects in the proximity of the RA. The domain was discretized using triangular stabilised elements with a remeshing technique activated when a prescribed threshold of the non-local plastic strain variable was reached. Mechanical and hydraulic boundary conditions of the model are also represented in Fig. 3c. A pull-out test was replicated by applying a vertical displacement with a monotonic and constant rate of 0.045D/s at the top of the anchor, where D is the diameter of the shaft. This value was selected to reach 10% D displacement, a common benchmark in pile design to delineate the limit state load. Three locations (A, B, and C) are selected on the anchor fingers, which are used for a more in-depth analysis in section 4.1.1.

Model parameters were calibrated from triaxial test data on Berea sandstone by Wong et al. (1992), following the calibration framework

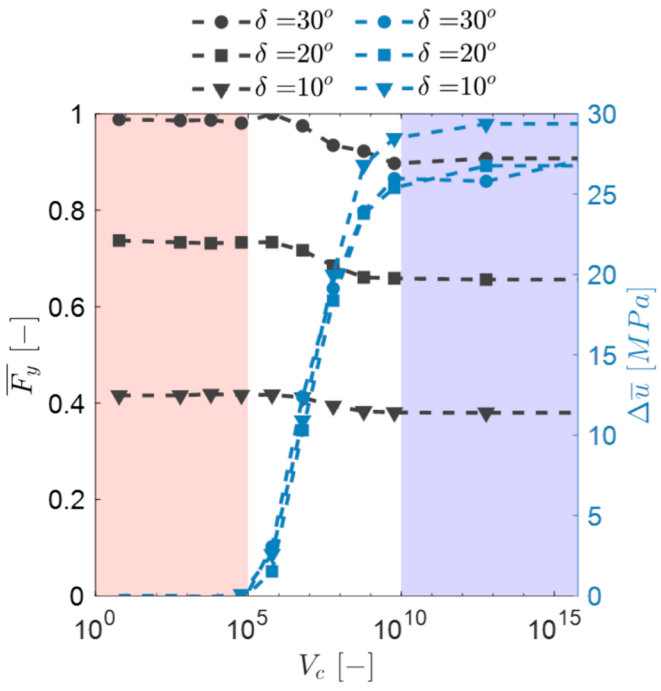

Fig. 5. Evolution of normalised vertical pull-out capacity (in black) and mean excess pore water pressure on the anchor fingers (in blue) with V_c at 10% D of axial displacement for $\delta = 10^{\circ}$, 20°, and 30°.

established by Ciantia and Di Prisco (2016). The calibration was conducted by adjusting the yield surface parameters to match the yield locus shape with experimental yield points as depicted in Fig. 4a. The plastic potential parameters were calibrated from the $d-\eta^*$ plot shown in Fig. 4b referring to the same drained triaxial tests under various isotropic confining pressures (120, 250, and 450 MPa). To calibrate the elastic and hardening parameters stress–strain curves of the same triaxial tests were used. Fig. 4c and Fig. 4d show such the model response against the experimental results.

The constitutive model presented in this paper is capable to broadly capture the triaxial experimental data on the Berea sandstone. For a better match with experimental data, more complex yield and plastic potential surfaces can be used. For example, Buscarnera and Laverack (2014), using the Lagioia and Nova (1995) surface, fitted the high confinement Berea sandstone response better. It should however be noted that in the numerical simulations of RA pullout, stress paths are typically in the low confinement zone (Fig. 9), hence yielding is typically occurring in the dilatant shear part ($\eta^* > M_{CS}$) where the model captures the available data more accurately (Fig. 9). As the goal of the paper is to investigate hydro-mechanical effects on RA pullout response a simpler model was chosen.

The calibrated constitutive model parameters are listed in Table 2. For the rock-anchor contact behaviour, an elasto-plastic law was used. Following Genco et al. (2022) the penalty parameter was selected to prevent numerical instability. The interface friction angle δ was varied for the analyses performed. The values of δ were taken such that typical rock steel interface values, such as the ones in Table 1, could be matched.

The numerical programme is summarised in Table 3 with the following sets of analyses:

- Pull-out simulations with rock permeability ranging from 1×10^{-18} m/s to 1×10^{-3} m/s (V_c ranging from $\simeq 6\text{x}10^5$ to $\simeq 6 \times 10^{15}$) with reference interface friction angle$\delta = 10^{\circ}$, 20°, and 30°
- Pull-out simulations with embedment depth ratio ranging from 2 to 10, and fingers inclination respect to the vertical axis (α) from 3 to 15° with anchor Young's moduli of 2.1×10^7 kPa, 11.5×10^7 kPa, and 2.1×10^8 kPa

4. Results

4.1. Rate effect investigation on RA performance

This section explores the role of rate of loading on RA performance. As already mentioned, rate effects are analysed by maintaining a constant pullout velocity (0.045D/s) while varying rock permeability.

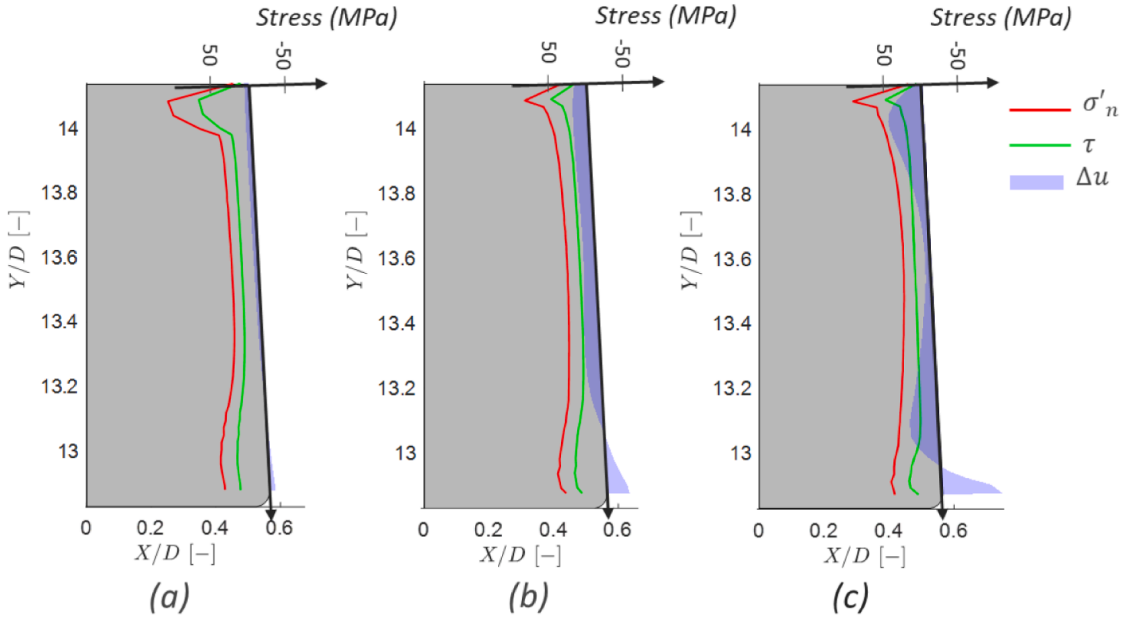

Fig. 6. Distribution of the effective (σ'_n), tangential stress (τ), and excess pore water pressure (Δu) acting on the anchor along the bottom part of the rock anchor for rock permeability of (a) $k = 1 \times 10^{-8}$ m/s ($V_c \simeq 6 \times 10^5$), (b) $k = 1 \times 10^{-9}$ m/s ($V_c \simeq 6 \times 10^6$), and (c) $k = 1 \times 10^{-10}$ m/s ($V_c \simeq 6 \times 10^7$), for the partially drained regime and reference interface friction angle.

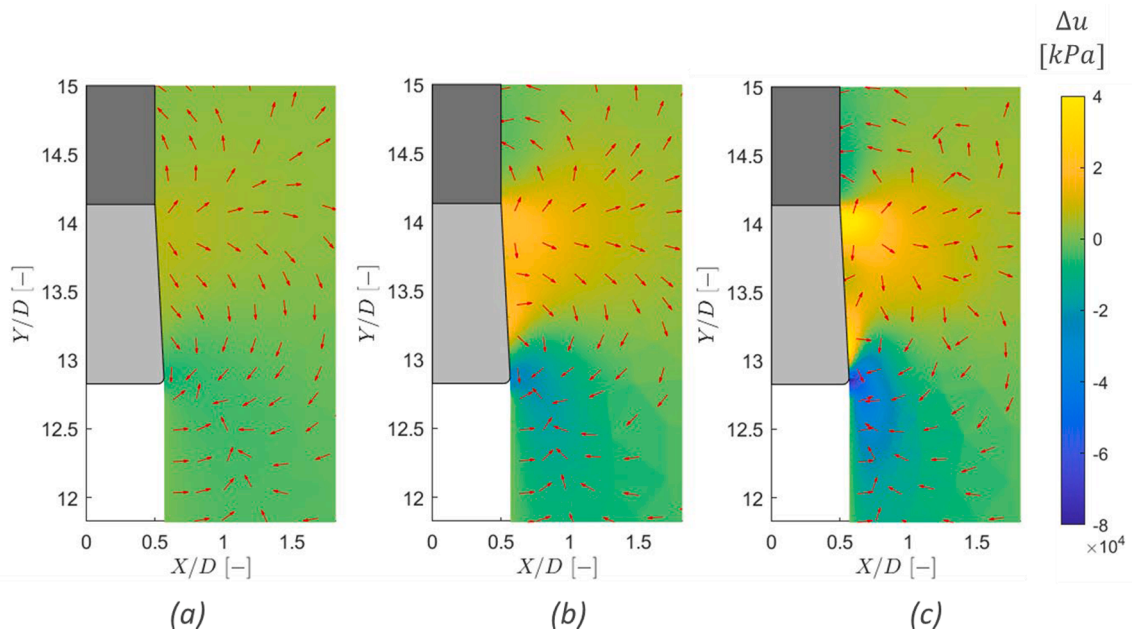

Fig. 7. Excess pore water pressure contours and Darcy' flow water vectors in the vicinity of the bottom part of the rock anchor for rock permeability values of (a) $k = 1 \times 10^{-8}$ m/s ($V_c \simeq 6 \times 10^5$), (b) $k = 1 \times 10^{-9}$ m/s ($V_c \simeq 6 \times 10^6$), and (c) $k = 1 \times 10^{-10}$ m/s ($V_c \simeq 6 \times 10^7$), for the partially drained regime and reference interface friction angle and embedment ratio adopted.

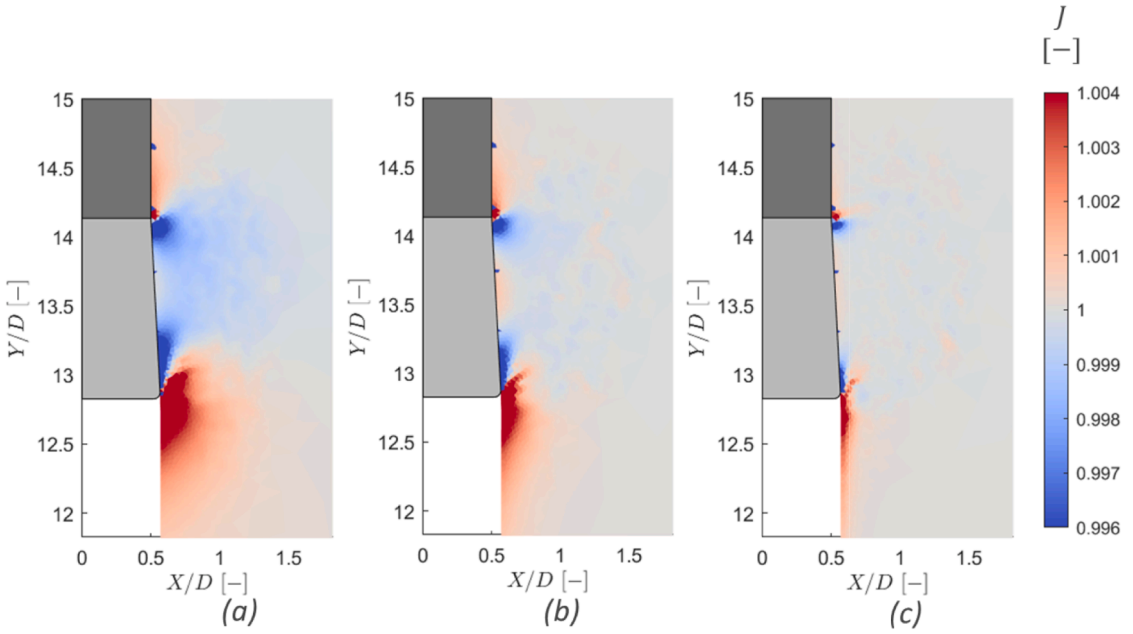

Fig. 8. Jacobian of the deformation gradient contour colourmap in the vicinity of the bottom part of the rock anchor for rock permeability values of (a) $k = 1 \times 10^{-8}$ m/s ($V_c \simeq 6 \times 10^5$), (b) $k = 1 \times 10^{-9}$ m/s ($V_c \simeq 6 \times 10^6$), and (c) $k = 1 \times 10^{-10}$ m/s ($V_c \simeq 6 \times 10^7$), for the partially drained regime and reference interface friction angle and embedment ratio adopted.

Variable interface friction angles δ were also examined. Permeability was assumed isotropic, varying from 1×10^{-18} m/s to 1×10^{-3} m/s, ecompassing the entire spectrum of drainage conditions and reflect the sandstone hydraulic properties as reported by Zhu and Wong (1997). In this way both undrained and perfectly drained regimes were considered. To quantify rate of loading, the normalized velocity V_c proposed by Randolph and Hope (2004) was used:

$$V_c = \mathrm{v}D/c_h = \lambda\gamma_w \mathrm{v}D/\dot{\sigma}_{v0}(1+e_0)k \tag{9}$$

v is the pull-out velocity, D the anchor shaft diameter, c_h the horizontal coefficient of consolidation, λ the compressibility index, γ_w the bulk water density, e_0 the initial void ratio, $\dot{\sigma}_{v0}$ the effective vertical stress and k the permeability. To capture the impact of interface friction on HM-RA behavior, three distinct interface friction angles (10°, 20°, and 30°), were considered, based on experimental findings by Ziogos et al. (2021)

Fig. 5 summarizes the results of the parametric analysis, displaying

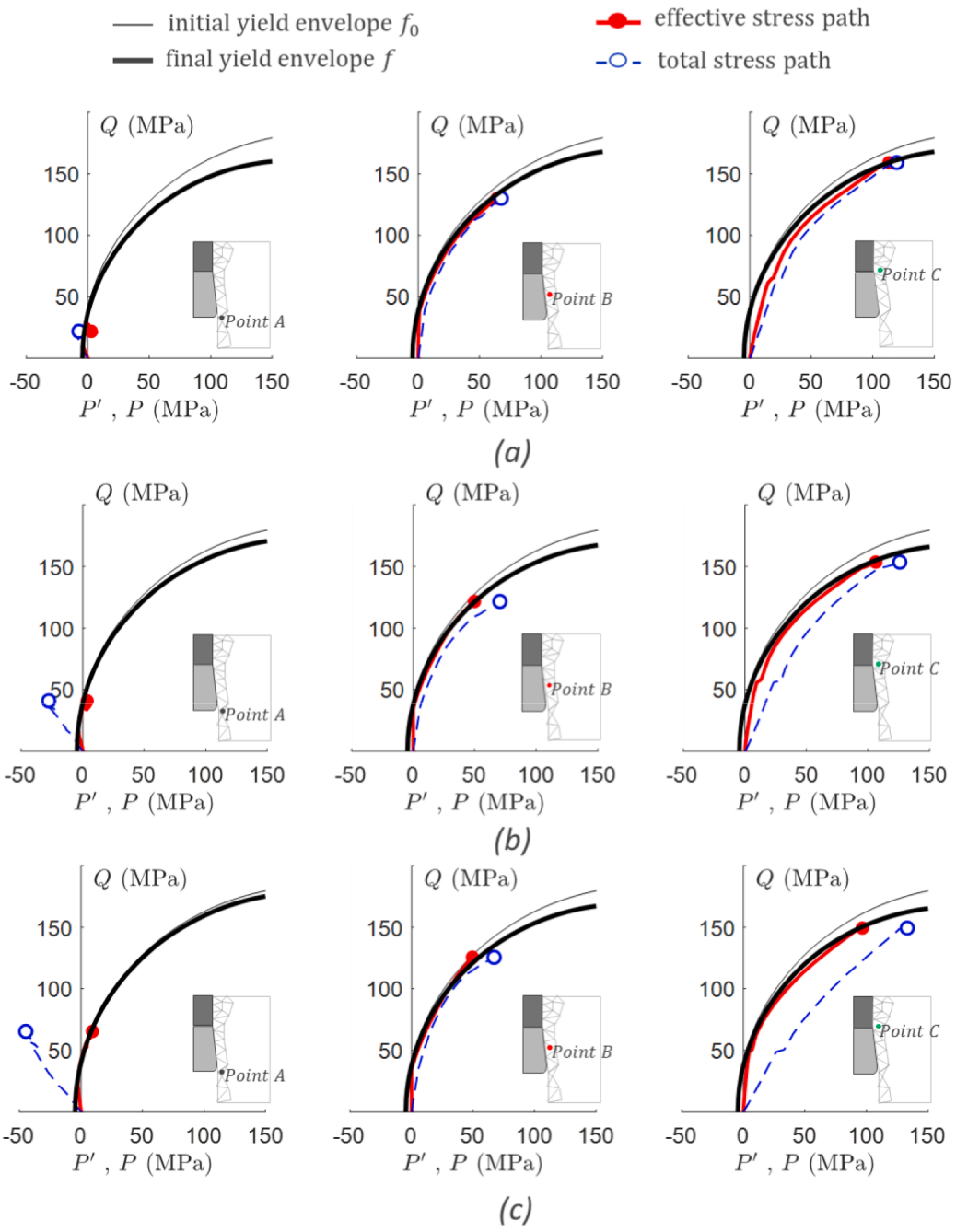

Fig. 9. Stress paths related to three points (Point A, Point B, and Point C respectively from left to right) of the region of interest for permeability values of (a) $k = 1 \times 10^{-8}$ m/s ($V_c \simeq 6 \times 10^5$), (b) $k = 1 \times 10^{-9}$ m/s ($V_c \simeq 6 \times 10^6$), and (c) $k = 1 \times 10^{-10}$ m/s ($V_c \sim \simeq 6 \times 10^7$), for the partially drained regime and reference interface friction angle and embedment ratio adopted with schematic of the location of the three points.

the normalized total pull-out capacity ($\overline{F}_y$) and change in mean excess water pressure ($\Delta\overline{u}$) acting on the anchor fingers against V_c at 10 %D of anchor displacement. The pullout force is normalised for confidentiality issues. When V_c is greater than $\simeq 6 \times 10^{10}$ the pull-out velocity ratio and the rock permeability are such that the response is undrained (i.e. this is evident in Figs. 7 and 8). On the other hand, when V_c is lower than $\simeq 6 \times 10^5$ the rock permeability is low enough to induce a drained response. Whereas, for V_c between these values a partially drained response is evident. Therefore, as shown in Fig. 5, as V_c increases (i.e. reducing the rock permeability) the pull-out capacity transitions from drained to undrained regime.

The findings distinctly show the impact of drainage conditions on RA capacity, demonstrating a decrease from drained to undrained states regardless of the interface friction angle adopted.

A notable reduction in pull-out capacity of approximately 15%, 10%, and 6% is registered in this regime for $\delta = 30°$, δ=20°, and $\delta = 10°$ respectively. The reduction in RA capacity with decreasing interface friction angle is highlighted, reaching up to 55% when transitioning from $\delta = 30°$ to $\delta = 10°$. The analysis also reveals a large increase in excess pore water pressure in partially drained condition, with $\Delta\overline{u}$ increments up to 15% registered as the interface friction angle increases. This underscores the significant influence of both the interface friction angle and excess pore water pressure on the pull-out capacity, emphasizing the necessity of incorporating these factors into design

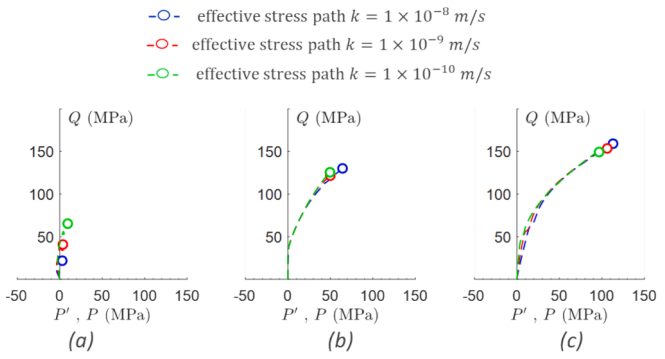

Fig. 10. Comparison of the effective stress path of Points A, B, and C, respectively from left to right at the different rock permeability values examined.

methodologies for RAs systems.

Fig. 6 shows the normal, tangential stresses, and excess of pore water pressure, at the bottom part of the anchor, for the rock permeability values examined within the partially drained regime for the reference interface friction angle at 10% D anchor displacement. This figure shows the distribution of the stresses along the bottom part of the anchor that contribute to the pull-out capacity due to the frictional nature of the large strain interaction problem. The plots presented herein are scaled enabling the comparison between the rock permeability values examined. Additionally, it is observed the presence of a peak value of the stresses at the edges of the anchor fingers describing a concave distribution regardless of the rock permeability value. The maximum value was observed at the top edge of the conical part of the anchor indicating the concentration of stress in an adjacent rock portion because of the axial anchor displacement. Furthermore, the interface friction angle adopted affects the orientation of the contact forces as expected. It should also be noted that at the bottom edge of the anchor the excess of pore water pressure distribution assumes negative values, conversely than the mid and top part of the anchor irrespective the rock permeability. This is further investigated in the subsequent paragraph.

4.1.1. The coupled HM response of RAs under axial loading

This section reports the spatial distribution of the excess pore water pressure, contractive or dilative response, and the stress paths in the partially drained regime for the RA pull-out case examined at 10% D anchor displacement. Assuming as reference interface friction angle $\delta = 30^{\circ}$ and embedment depth $H/D = 6$, the results highlight how strain propagation impacts the pore water pressure distribution, causing the formation of the deep failure mechanism (based on the value of embedment depth assumed). Fig. 7 illustrates the variations in excess pore water pressure and the Darcy's flow water for permeabilities of $k = 1 \times 10^{-8}$ m/s ($V_c \simeq 6 \times 10^5$), $k = 1 \times 10^{-9}$ m/s ($V_c \simeq 6 \times 10^6$), and $k = 1 \times 10^{-10}$ m/s ($V_c \simeq 6 \times 10^7$), focusing on a Region of Interest (ROI) extended radially up to 2D and axially up to 3.2D representing a zone in proximity of the conic part of the anchor.

A key observation is the formation of negative changes of pore water pressure in parts of this ROI, with magnitude increasing as the rock permeability is reduced. This negative excess of pore water pressure is

Table 4
Table summarising the main results for varying H/D (fixed α) for displacement of 45%D.

H/D (−)	E (kPa)	α (°)	$\overline{F}_{ymax}$ (−)
2			0.94
4			0.99
6	2.1×10^8	3	1.00
8			0.99
10			0.99

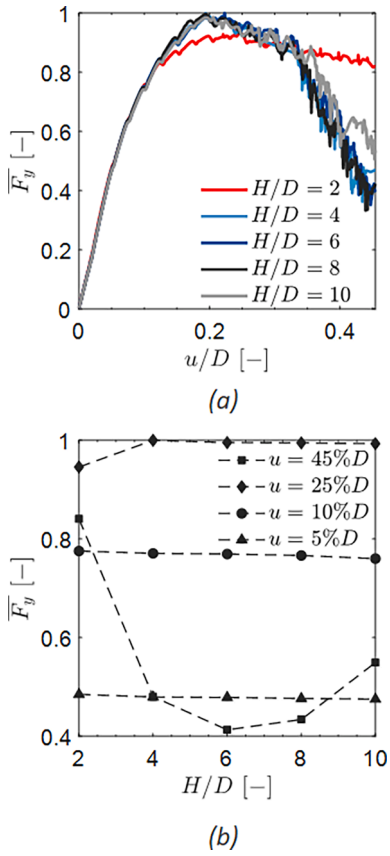

Fig. 11. a) Normalised pull-out capacity with the axial displacement and b) normalised pull-out capacity with the normalised embedment depth for four levels of displacements (5% D, 10% D, 25% D, and 45% D).

confined to a narrow zone at the outer edge of the fingers, peaking at that edge.

It should be noted that, the pore water pressure changes that develop at the bottom edge of the anchor, particularly in the undrained scenarios, reach high negative values (up to −80 MPa). This happens because of the stress dilatancy rule of the MCC model that may overestimate realistic dilatancy values as η^* increases. In fact, failure in this region occurs because of shear at very low P' (see the stress paths were in Fig. 9) where the model dilatancy reaches very high values ($\eta^* \simeq 10$). Therefore, dilatation which is observed at the bottom edge of the anchor tends to localise at the outer edge of the fingers of the anchor increasing the pore space volume and hence explaining the distribution of negative pore water pressure changes, whereas contractive behaviour is evident at the centre of the conic part of the anchor. The negative *pwp* generated would still have a limit imposed by cavitation (−120 MPa at ambient conditions (Magaletti et al., 2021)) which is however not reached in any of the simulations. Nonetheless these high negative values would anyways be unrealistic as i) permeability increases due to rock dilatation and ii) rock damage generates preferential paths for water. These two important features that for sake of simplicity are not accounted in the model, would enhance dissipation and, if taken into account, most likely prevent the generation of these very large negative pressures.

The formation of a bulb of increased pore water pressure is more evident for the intermediate rock permeability value, which remain relatively stable in size during the analysis, whereas reducing the rock permeability results in a more localised distribution as shown in Fig. 8.

The presence of negative excess pore water pressure can be further explained showcasing the volumetric plastic strain expressed by the contour of the Jacobian J of the deformation gradient depicted in Fig. 8. When the value of J is higher than 1 it implies dilatation, when lower

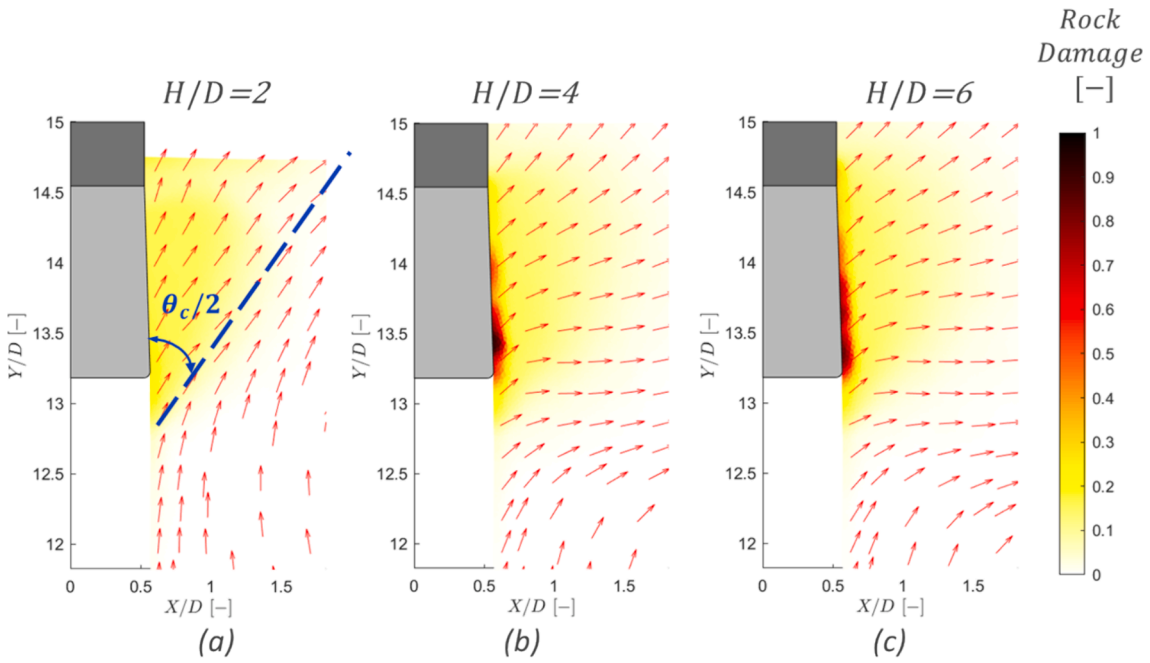

Fig. 12. Contour of the rock damage and rock displacement vectors (in red) extracted for three values of embedment ratio: (a) $H/D = 2$, (b) $H/D = 4$, and (c) $H/D = 6$ at the maximum value of axial displacement achieved by the simulations (45% D).

Table 5
Table summarising the main results due to varying α (fixed H/D) for 45%D as level of displacement.

H/D (−)	E (kPa)	α (°)	$\overline{F}_{ymax}$ (−)
6	2.1×10^8	3	0.21
		6	0.32
		10	0.55
		15	1.00
6	11.5×10^7	3	0.21
		6	0.32
		10	0.54
		15	0.98
6	2.1×10^7	3	0.20
		6	0.30
		10	0.48
		15	0.86

than 1 it contraction. Therefore, dilatation which is observed at the bottom edge of the anchor tends to localise at the outer edge of the fingers of the anchor increasing the pore space volume and hence explaining the distribution of negative pore water pressure changes, whereas contractive behaviour is evident at the centre of the conic part of the anchor. To complete the coupled HM characterization and quantify the evolution of the excess pore water pressure, the stress paths were plotted at three points (Point A, Point B, and Point C) localised at the bottom, mid, and upper part of the cone anchor illustrated in Fig. 9. The points were selected as representative of the dilatant and contractant zones. This figure shows the initial and final yield envelope of the S-MCC model presented (outlined by continuous black lines). The total and effective stress paths are depicted in the figure (using dotted blue and continuous red lines, respectively). The presence of negative excess pore water pressure is highlighted from the stress path at the Point A for different rock permeability values examined. Specifically, the total stress path is herein located at left of the effective stress path. The distance between them indicates the excess of pore water pressure which at the Point A increases from 10.1 MPa to 54.16 MPa from the lowest to the highest rock permeability value considered. On the contrary, for the Point B and C, which are located inside the bulb of the contractive zone, the total stress path lies on right side of the effective stress path. Specifically, the distance between them increases reducing the rock permeability. Additionally, at Point C the positive value of excess pore water pressure increasing from 6.31 MPa to 36.46 MPa from the lowest rock permeability to the highest in the partially drained regime. A noteworthy observation is the contraction of the yield surface in the plastic regime, a phenomenon induced by the rock destructuration process leading to the reduction of the P_t. The effective stress path plots help in explaining the increase of the pull-out capacity from the undrained to the drained regime visible in Fig. 6. The main strength contribution of the anchor comes from the shear strength mobilization at B and C. As visible in Fig. 10b and c, the effective stress path of the undrained model is lower than the one of the drained one for both points (which contributes to the mobilization of the rock strength). This means that the rock can mobilise higher strengths increasing the permeability. At point A (Fig. 10a), because of the large negative excess pore water pressure, the effective stress path has the opposite trend. However, for clear geometrical reasons, the mobilised strength in this zone does not contribute to the axial strength.

4.2. Geometry influence on RA performance

This section presents the results of the numerical investigation of geometry, and its impact on rock anchor performance. Results of rock anchor performance for variable embedment depths and variable finger inclination angles are herein presented. For all cases $k = 1 \times 10^{-12}$ m/s ($V_c \simeq 6 \times 10^9$), (undrained regime) was used. To investigate the extent of damage in the simulations, a Rock Damage (RD) variable, defined as $D = 1 - (P_t/P_{t0})$, where P_{t0} indicates the initial tensile strength, was used.

4.2.1. Embedment depth effect on the RA performance

The role of the H/D in determining the load capacity and the failure mode of RAs is investigated by varying the embedment depth from 2 to 10, while keeping the rock permeability and interface friction constant. Results are normalized against the maximum value reached by the simulations for commercial confidentiality, facilitating the comparison of normalised pull-out capacity ($\overline{F}_y$) across different embedment ratios.

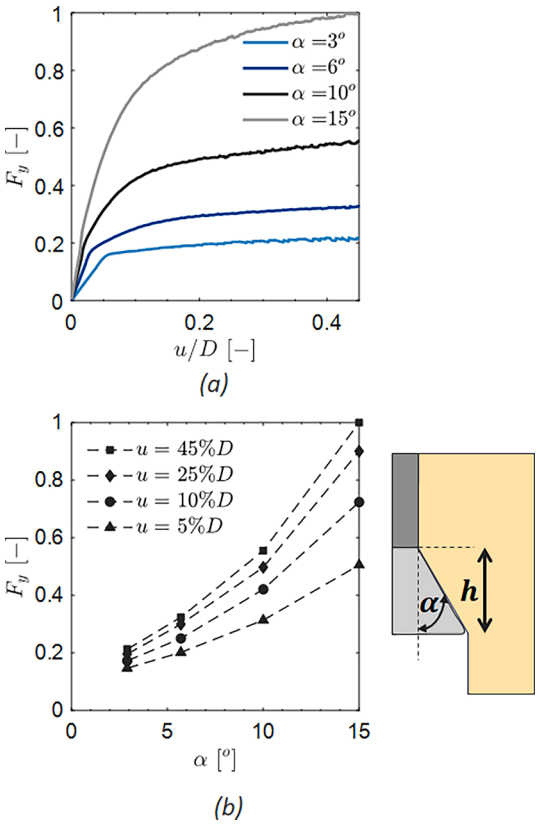

Fig. 13. a) normalised load displacement curves for variable α and b) normalized pull-out capacity for four levels of displacements (5% D, 10% D, 25% D, and 45% D) with schematic of the conical part of the anchor.

Table 4 summarizes the set of simulations performed.

Fig. 11b illustrates the variation of anchor capacity $\overline{F}_{y,max}$ with embedment depth, revealing that up to 10% D axial displacement, no significant difference in pull-out capacity emerges. This effect is attributed to the elastic behaviour exhibited by the rock-anchor system at lower displacement levels, where all load–displacement curves show similar stiffness (Fig. 11a).

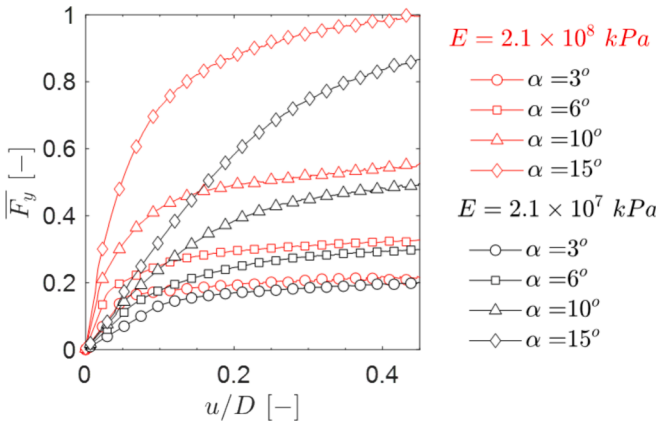

Fig. 15. Normalised load displacement curves for variable α and Young's modulus.

At 25% D as displacement level, the influence of H/D begins to emerge and an increase in the $\overline{F}_y$ is observed from an embedment ratio of 2 to 4 as depicted in Fig. 11b. Beyond this range, a plateau indicates that further increasing the embedment depth does not contribute to additional anchor capacity, in line with findings by Cerfontaine et al. (2021). However, as axial displacement increases over 25% D, as peak capacity is reached or exceed and then the load capacity decreases up to the maximum value of displacement achieved, showing a softening behaviour regardless of the embedment depth considered.

Fig. 12 shows the rock damage distribution and the displacement vectors in the ROI for varying H/D ratios at large displacements (45% D). At the lowest embedment ratio (H/D = 2), the classic cone-failure mode emerges, extending towards the top boundary of the rock with a cone inclination (θ_c) of approximately 55° (assuming the entire rock anchor domain). The displacement vectors scaled shown are in line with the configuration of the cone pulled out and are directed in parallel to the failure surface (represented by the blue dotted line in Fig. 12a). The maximum value of the RD registered is 23.5% which is near

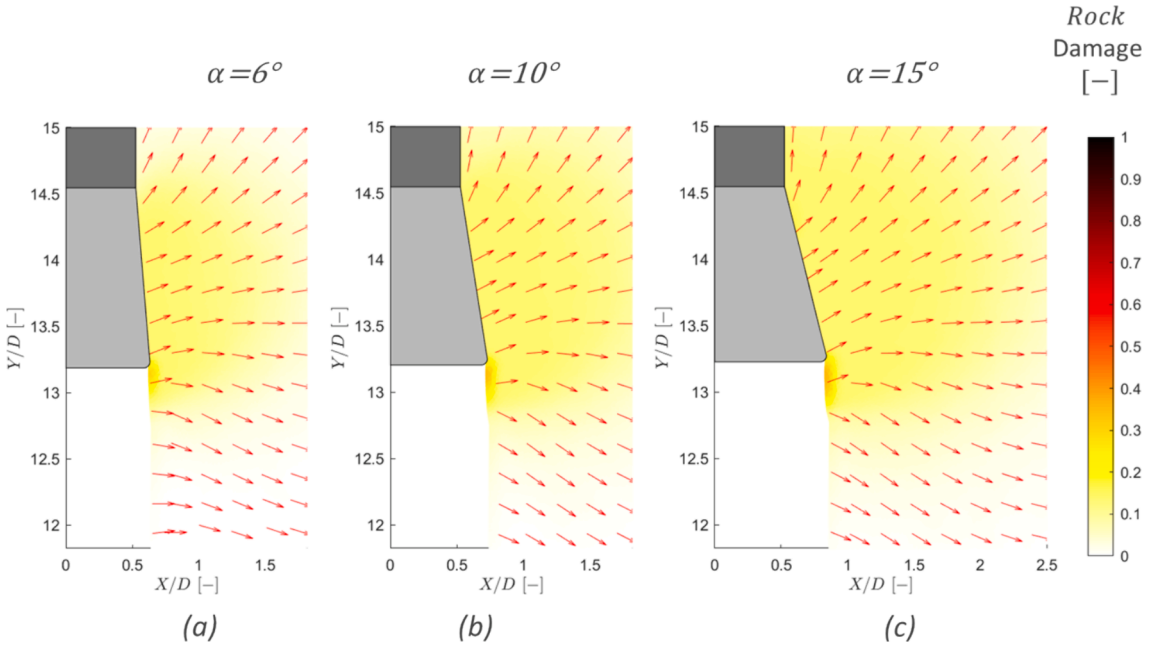

Fig. 14. Contour of the rock damage and rock displacement vectors extracted for three values of α: (a) $\alpha = 6^{\circ}$, (b) $\alpha = 10^{\circ}$, and (c) $\alpha = 15^{\circ}$, at the maximum value of axial displacement achieved (45% D).

homogeneously distributed inside the rock cone. A deep failure mechanism is exhibited once the depth exceeds the H/D of 4. This deep mechanism is characterized by the localisation of plastic strains at the interface with anchor fingers and not as the wide wedge mechanism observed in clays (Charlton et al., 2016). This is further highlighted by the rock displacement vectors, that show significant vertical movement only in proximity of the anchor fingers (Fig. 12b and c). The RD reaches the maximum value near to the outer edge of the fingers for the intermediate and highest embedment depth which indicates that the rock becomes almost destructured (Fig. 12b and c). The main results in term of load capacity are synthesized in Table 4.

4.2.2. *Influence of the anchor finger inclination on the RA performance*

The numerical investigation focuses on exploring how the deep failure mechanism changes with geometry and stiffness of the anchor. The inclination angle was varied from 3 to 15° and different rock anchor Young's moduli were considered (Fig. 15), while keeping rock permeability, embedment depth, and interface friction angle constant (as detailed in Table 5). The contact domain approach was used to describe the rock-anchor contact.

Fig. 13 illustrates how α impacts the pull-out capacity keeping constant the stiffness of the anchor at displacement levels of 5% D, 10% D, 25% D, and 45% D. An increase in load capacity was observed with the inclination of the fingers for all displacement levels considered. The stiffness of the load–displacement curves tends to increase with the inclination of the fingers as observed in Fig. 13a.

The configuration of the deep failure mechanism by means of the contour plot of the rock damage at 45% D for α angles of 6°, 10°, and 15° is represented in Fig. 14. The failure mechanism observed remains unaffected by the inclination of the conical part of the anchor. However, the radial extension of the damage zone expands with the inclination of the lateral face. This extension ranges from 1.5D to 2.5D as α increases from 6° to 15°. Despite the inclination, deviatoric plastic strains are manly concentrated at the bottom corner of the anchor, attributed to the presence of inclined fingers.

Fig. 15 illustrates the effect of the anchor stiffness and the inclination of the fingers on the normalised pull-out capacity up to 45% D as level of displacement. This figure indicates a non-linear increase of the anchor capacity with the Young's modulus for the inclinations of the fingers considered. Furthermore, the different stiffness of the load displacement curves was observed affecting the axial capacity of the rock anchor. Finally, the increase of the anchor stiffness and inclination of the fingers may lead to the increase of the anchor capacity optimizing the anchor geometry and reducing the overall cost of the anchoring system.

5. Conclusions

This paper employs a coupled hydro-mechanical continuum formulation to explore the influence of rate effects on the axial capacity of a novel design for self-installing, steel-groutless anchors adopted for offshore renewable applications. The anchor geometry is here simplified to a straight shaft with a conical base designed to reflect radially expanding rock engagement fingers found at the base of the real anchor.

The study of rock permeability variation highlights that anchor capacity decreases with normalized pullout velocity when moving from the drained to the undrained regime, regardless of the interface friction angle. However, this transition may be affected by the formation of a zone of negative pore water pressure change at the bottom corner of the anchor. It was found that this phenomenon occurs because of shear failure at very low P'. The magnitude of Δu will therefore depend on the ability of the model to capture the dilative response of the rock, the formation of cracks and consequent preferential paths for water and in some circumstances (low permeability or fast pullout) the ability to incorporate cavitation phenomena that may incur. Further experimental and numerical study on this mechanism is encouraged. While interface friction also leads to a linear increase in capacity, regardless of the hydraulic state, this effect is primarily observed in cone pull-out and deep failure modes.

Parametric analysis of the embedment ratio similarly highlights a linear trend on the axial anchor capacity, until the failure mode shifts to deep-failure and the capacity plateaus. In this scenario, anchor capacity is controlled by the inclination of the bottom part of the anchor, with wider failure surfaces induced by finger inclination following a linear and exponential trend respectively for low (lower than 3°) and high inclination (greater than 3°) of the fingers at the bottom of the anchor. The results presented in this paper show the critical role of anchor geometry on failure distribution, distinguishing between shallow and deep failure modes by means of the large strain numerical models performed. This distinction is crucial for accurately estimating the load capacity of RAs, suggesting that conventional cone pull-out models may overestimate capacity for deeper embedment. Consequently, a novel design approach, attuned to the nuances of deep failure configurations, is essential. These findings highlight the potential for geometric optimization of the anchor design, aiming to maximize load capacity while potentially reducing the overall costs associated with the anchoring system.

CRediT authorship contribution statement

Alessio Genco: Writing – review & editing, Writing – original draft, Software, Investigation, Formal analysis, Methodology. **Matteo Oryem Ciantia:** Conceptualization, Writing – review & editing, Software, Resources, Supervision, Funding acquisition, Project administration. **Marco Previtali:** Writing – review & editing, Software, Investigation. **Michael Brown:** Writing – review & editing, Supervision. **Ana Ivanovic:** Writing – review & editing, Supervision. **Nick Cresswell:** Writing – review & editing, Supervision. **Vincent Twomey:** Writing – review & editing.

Declaration of competing interest

The authors declare that they have no known competing financial interests or personal relationships that could have appeared to influence the work reported in this paper.

Data availability

Data will be made available on request.

Acknowledgements

This research is part of an industry funded studentship (ETP EIDP #182). The technical and financial support of the industrial partner SCHOTTEL Marine Technologies and the financial support of the Engineering Technology Partnership (ETP) are gratefully acknowledged. The ICE-PICK project (EP/W00013X/1) supporting the third author is also acknowledged.

References

Bagdassarov, N., 2021. Permeability of rocks. Fundament. Rock Phys. 178–210 https://doi.org/10.1017/9781108380713.006.

Brown, E.T., 2015. Rock engineering design of post-tensioned anchors for dams – a review. J. Rock Mech. Geotech. Eng. 7 (1), 1–13. https://doi.org/10.1016/j.jrmge.2014.08.001.

Brown, M.J., Hyde, A.F.L., 2008. Rate effects from pile shaft resistance measurements. Can. Geotech. J. 45 (3), 425–431. https://doi.org/10.1139/T07-115.

Buscarnera, G., Laverack, T., 2014. Path dependence of the potential for compaction banding: theoretical predictions based on a plasticity model for porous rocks. AGU: J Geophys Res Solid Earth 119, 3678–3699. https://doi.org/10.1002/2013JB010562. Received.

Carbonell, J.M., Monforte, L., Ciantia, M.O., Arroyo, M., Gens, A., 2022. Geotechnical particle finite element method for modeling of soil-structure interaction under large deformation conditions. J. Rock Mech. Geotech. Eng. 14 (3), 967–983. https://doi.org/10.1016/J.JRMGE.2021.12.006.

Cerfontaine, B., Brown, M. J., Caton, A., Hunt, A., Cresswell, N., 2021. Numerical modelling of rock anchor uplift capacity for offshore applications. 14th European Wave & Tidal Energy Conference (EWTEC). https://proceedings.ewtec.org/product/ewtec-2021-plymouth-uk/.

Charlton, T.S., Rouainia, M., Gens, A., 2016. Numerical analysis of suction embedded plate anchors in structured clay. Appl. Ocean Res. 61, 156–166. https://doi.org/10.1016/j.apor.2016.10.009.

Chow, S.H., Diambra, A., O'loughlin, C.D., Gaudin, C., Randolph, M.F., 2020. Consolidation effects on monotonic and cyclic capacity of plate anchors in sand. Geotechnique 70 (8), 720–731. https://doi.org/10.1680/jgeot.19.TI.017.

Ciantia, M.O., Di Prisco, C., 2016. Extension of plasticity theory to debonding, grain dissolution, and chemical damage of calcarenites. Int. J. Numer. Anal. Meth. Geomech. 40 (3), 315–343. https://doi.org/10.1002/nag.2397.

Ciantia, M. O., 2018. A constitutive model for the hydro-chemo-mechanical behaviour of chalk. Engineering in Chalk - Proceedings of the Chalk 2018 Conference, January, 275–281. https://doi.org/10.1680/eiccf.64072.275.

Coates, D. F., Yu, Y. S., 1971. Rock anchor design mechanics. Mines Branch Research Report R 233. Ottawa: Information Cnada 1970. https://ostrnrcan-dostrncan.canada.ca/entities/publication/d120f72b-5e4c-4381-bbd3-001aa4081fe7.

Cresswell, N., Hayman, J., Kyte, A., Hunt, A., Jeffcoate, P., 2016. Anchor Installation for the Taut Moored Tidal Platform PLAT-O. 3rd Asian Wave and Tidal Energy Conference, October 2016. https://s3-eu-west-1.amazonaws.com/assets-sustainablemarine-com/downloads/AWTEC-2016-Anchoring-Paper.pdf.

Dadvand, P., Rossi, R., Oñate, E., 2010. An object-oriented environment for developing finite element codes for multi-disciplinary applications. In Archives of Computational Methods in Engineering (Vol. 17, Issue 3). https://doi.org/10.1007/s11831-010-9045-2.

De Borst, R., Vermeer, P.A., 1985. Possibilities and limitations of finite elements for limit analysis. Geotechnique 35 (1), 90–94. https://doi.org/10.1680/geot.1985.35.1.90.

Drescher, A., Detournay, E., 1993. Limit load in translational failure mechanisms for associative and non-associative materials. Geotechnique 43 (3), 443–456. https://doi.org/10.1680/geot.1993.43.3.443.

Frost, J.D., DeJong, J.T., Recalde, M., 2002. Shear failure behavior of granular-continuum interfaces. Eng. Fract. Mech. 69 (17), 2029–2048. https://doi.org/10.1016/S0013-7944(02)00075-9.

Galavi, V., Schweiger, H.F., 2010. Nonlocal multilaminate model for strain softening analysis. Int. J. Geomech. 10 (1), 30–44. https://doi.org/10.1061/(asce)1532-3641(2010)10:1(30).

Genco, A., Ciantia, M. O., Ivanovic, M. B. A., Caton, A., Cresswell, N., 2022. G-PFEM Numerical Assessment of Rock Anchor Interface Properties on Pull-Out Capacity for Renewable Offshore Applications. In: Ferrari, A., Rosone, M., Ziccarelli, M., Gottardi, G. (eds) Geotechnical Engineering in the Digital and Technological Innovation Era. CNRIG 2023. Springer Series in Geomechanics and Geoengineering. Springer, Cham. https://doi.org/10.1007/978-3-031-34761-0_52.

Griffiths, D.V., Lane, P.A., 1999. Slope stability analysis by finite elements. Geotechnique 49 (3), 387–403. https://doi.org/10.1680/geot.1999.49.3.387.

Hill, R., 1962. Acceleration waves in solids. J. Mech. Phys. Solids 10 (1), 1–16. https://doi.org/10.1016/0022-5096(62)90024-8.

Huněk, I., 1993. On a penalty formulation for contact-impact problems. Comput. Struct. 48 (2), 193–203. https://doi.org/10.1016/0045-7949(93)90412-7.

Kim, H.K., Cho, N.J., 2012. A design method to incur ductile failure of rock anchors subjected to tensile loads. Electron. J. Geotech. Eng. 17 T, 2737–2746.

Lagioia, R., Nova, R., 1995. An experimental and theoretical study of the behaviour of a calcarenite in triaxial compression. Geotechnique 45 (4), 633–648. https://doi.org/10.1680/geot.1995.45.4.633.

Lei, X., Tamagawa, T., Tezuka, K., Takahashi, M., 2011. Role of drainage conditions in deformation and fracture of porous rocks under triaxial compression in the laboratory. Geophys. Res. Lett. 38 (24), 1–5. https://doi.org/10.1029/2011GL049888.

Littlejohn, G.S., Bruce, D.A., Deppner, W., 1978. Anchor field test in carboniferous strata. Rev. Fr. Geotech 3, 82–86. https://www.geotechnique-journal.org/articles/geotech/abs/1978/01/geotech1978003p82/geotech1978003p82.html.

Magaletti, F., Gallo, M., Casciola, C.M., 2021. Water cavitation from ambient to high temperatures. Sci. Rep. 11 (1), 1–10. https://doi.org/10.1038/s41598-021-99863-z.

Mánica, M.A., Gens, A., Vaunat, J., Ruiz, D.F., 2018. Nonlocal plasticity modelling of strain localisation in stiff clays. Comput. Geotech. 103 (March), 138–150. https://doi.org/10.1016/j.compgeo.2018.07.008.

Mánica, M.A., Ciantia, M.O., Gens, A., 2020. On the stability of underground caves in calcareous rocks due to long-term weathering. Rock Mech. Rock Eng. 53 (9), 3885–3901. https://doi.org/10.1007/s00603-020-02142-y.

Monforte, L., Carbonell, J.M., Arroyo, M., Gens, A., 2017. Performance of mixed formulations for the particle finite element method in soil mechanics problems. Computat. Particle Mech. 4 (3), 269–284. https://doi.org/10.1007/s40571-016-0145-0.

Monforte, L., Arroyo, M., Carbonell, J.M., Gens, A., 2018. Coupled effective stress analysis of insertion problems in geotechnics with the particle finite element method. Comput. Geotech. 101 (May), 114–129. https://doi.org/10.1016/j.compgeo.2018.04.002.

Monforte, L., Ciantia, M.O., Carbonell, J.M., Arroyo, M., Gens, A., 2019. A stable mesh-independent approach for numerical modelling of structured soils at large strains. Comput. Geotech. 116 (August), 103215 https://doi.org/10.1016/j.compgeo.2019.103215.

Oliynyk, K., Ciantia, M.O., Tamagnini, C., 2021. A finite deformation multiplicative plasticity model with non–local hardening for bonded geomaterials. Comput. Geotech. 137, 104209 https://doi.org/10.1016/J.COMPGEO.2021.104209.

Oliynyk, K., Ciantia, M.O., Tamagnini, C., 2024. Localization patterns emerging in CPTu tests in a saturated natural clay soil. Comput. Geotech. 137, 104209 https://doi.org/10.1016/j.compgeo.2024.106343.

Oñate, E., Idelsohn, S.R., Del Pin, F., Aubry, R., 2004. The particle finite element method — an overview. Int. J. Comput. Methods 01 (02), 267–307. https://doi.org/10.1142/s0219876204000204.

Panton, B., Elmo, D., Stead, D., Schlotfeldt, P., 2015. A discrete fracture network approach for the design of rock foundation anchorage. Trans. Inst. Min. Metall. Section A: Min. Technol. 124 (3), 150–162. https://doi.org/10.1179/1743286315Y.0000000014.

Previtali, M., Ciantia, M. O., Riccio, T., 2023. Numerical installation of OE piles in soft rocks within the G-PFEM framework. Proceedings of the 10th European Conference on Numerical Methods in Geotechnical Engineering, June, 322–328. https://doi.org/10.53243/NUMGE2023-322.

Serrano, A., Olalla, C., 1999. Tensile resistance of rock anchors. Int. J. Rock Mech. Min. Sci. 36 (4), 449–474. https://doi.org/10.1016/S0148-9062(99)00021-2.

Stanchits, S., Fortin, J., Gueguen, Y., Dresen, G., 2009. Initiation and propagation of compaction bands in dry and wet bentheim sandstone. Pure Appl. Geophys. 166 (5–7), 843–868. https://doi.org/10.1007/s00024-009-0478-1.

Weerasinghe, R. B., Littlejohn, G. S., 1997. Uplift capacity of shallow anchorages in weak mudstone. In Ground anchorages and anchored structures. Proc. conference, London, 1997.

Wong, T., Szeto, H., Zhang, J., 1992. Effect of Loading Path and Porosity on the Failure Mode of Porous Rocks. 45(8), 281–293. https://asmedigitalcollection.asme.org/appliedmechanicsreviews/article-abstract/45/8/281/421512/Effect-of-Loading-Path-and-Porosity-on-the-Failure?redirectedFrom=fulltext.

Wyllie, D. C., 1999. Foundations on Rock: Engineering Practice, Second Edition (2nd Editio). https://www.taylorfrancis.com/books/mono/10.1201/9781482295009/foundations-rock-duncan-wyllie.

Yap, L.P., Rodger, A.A., 1984. A study of the behaviour of vertical rock anchors using the finite element method. Int. J. Rock Mech. Min. Sci. 21 (2), 47–61. https://doi.org/10.1016/0148-9062(84)91173-2.

Zhang, Q., Feng, R., Xu, Z., Liu, S., Qian, J., 2019. Evaluation of ultimate pullout capacity of anchor cables embedded in rock using a unified rupture shape model. Geotech. Geol. Eng. 37 (4), 2625–2637. https://doi.org/10.1007/s10706-018-00782-0.

Zhao, L.H., Yang, X.P., Huang, F., Tang, Y.G., Hu, S.H., 2018. Variational analysis of the ultimate pullout capacity of shallow circular anchor plates in rock foundations based on the Hoek-Brown failure criterion. Int. J. Rock Mech. Min. Sci. 106 (January), 190–197. https://doi.org/10.1016/j.ijrmms.2018.04.027.

Zhu, W., Wong, T., 1997. The transition from brittle faulting to cataclastic flow: permeability evolution. J. Geophys. Res. Solid Earth 102 (B2), 3027–3041. https://doi.org/10.1029/96jb03282.

Ziogos, A.D., Brown, M.J., Ivanovic, A., Morgan, N., 2015. Rock-steel interface testing and considerations for gravity foundations for tidal energy generators. Frontiers in Offshore Geotechnics III - 3rd International Symposium on Frontiers in Offshore Geotechnics. ISFOG 2015, 1245–1250. https://doi.org/10.1201/b18442-188.

Ziogos, A., Brown, M. J., Ivanovic, A., Morgan, N., 2021. Understanding rock–steel interface properties for use in offshore applications. Proceedings of the Institution of Civil Engineers - Geotechnical Engineering, 1–15. https://doi.org/10.1680/jgeen.20.00183.